Magnetic structure and magnon dispersion in LaSrFeO₄

N. Qureshi,[1,*] H. Ulbrich,[1] Y. Sidis,[2] A. Cousson,[2] and M. Braden[1,†]

[1]*II. Physikalisches Institut, Universität zu Köln, Zülpicher Strasse 77, D-50937 Köln, Germany*
[2]*Laboratoire Léon Brillouin, C.E.A./C.N.R.S., F-91191 Gif-sur-Yvette Cedex, France*

We present elastic and inelastic neutron scattering data on LaSrFeO₄. We confirm the known magnetic structure with the magnetic moments lying in the tetragonal basal plane, but our macroscopic and neutron diffraction data do not reveal any additional magnetic phase transition connected to a spin reorientation or to a redistribution of two irreducible representations. Our inelastic neutron scattering data reveals the magnon dispersion along the main-symmetry directions [0 ξ 0] and [ξ -ξ 0]. The dispersion can be explained within linear spin-wave theory yielding an antiferromagnetic nearest-neighbor interaction parameter $J_1 = 7.4(3)$ meV and a next-nearest neighbor interaction parameter $J_2 = 0.4(3)$ meV. The dispersion is gapped with the out-of-plane anisotropy gap found at $\Delta_{\mathrm{out}} = 5.26(2)$ meV, while evidence is present that the in-plane anisotropy gap lies at lower energies, where it cannot be determined due to limited instrument resolution.

I. INTRODUCTION

Transition-metal oxides of the Ruddlesden-Popper series $R_{n+1}M_nO_{3n+1}$ (Ref. 1) exhibit a large variety of interesting physical properties, such as charge, spin, and orbital ordering, which are intimately coupled and may lead to fascinating phenomena like the colossal magnetoresistance in LaMnO₃ (Ref. 2) ($n = \infty$, "113" structure). The $n = 1$ compound LaSrMO₄ ("214" structure), a two-dimensional analog, reveals a single-layered perovskite structure of the K₂NiF₄ type [space group $I4/mmm$, Fig. 1(a)], where the O ions octahedrally coordinate the M ions to build perfect MO₂-square planes [Fig. 1(b)]. While in the 113 compounds these planes are vertically connected to form a three dimensional magnetic network, they are separated and shifted along $[\frac{a}{2} \frac{b}{2} 0]$ in the 214 compounds, which reduces their electronic dimensionality and renders these systems ideal for studying their orbital and magnetic correlations in a less complex environment. For M = (Mn, Fe, Co, Ni, Cu) all 214 systems are known to be charge-transfer insulators with an antiferromagnetic ground state.[3–10] The magnetic structures have been reported to exhibit collinear spin arrangements, where the nearest-neighbor spins are coupled antiferromagnetically and the next-nearest neighbor spins are coupled ferromagnetically. However, La₂CuO₄ (Refs. 9,10) and La₂NiO₄ (Ref. 8) exhibit slightly canted antiferromagnetic structures. LaSrFeO₄ orders magnetically at $T_N = 380$ K (Ref. 6), and two further magnetic phase transitions were reported as the susceptibility shows anomalies at 90 and 30 K (Ref. 11). These magnetic phase transitions are thought to originate from a redistribution of two collinear representations.[12] Magnetic excitations in layered transition metal oxides have attracted considerable interest in the context of both the high-temperature superconductors and the manganates exhibiting colossal magnetoresistance.[13] Rather intense studies on nickelates, manganates, and cobaltates with the K₂NiF₄ (214) structure have established the spin-wave dispersion for pure and doped materials. In the pure materials there is a clear relation between the orbital occupation and the magnetic interaction parameters, which may result in unusual excitations like in-gap modes.[14] Upon doping, almost all of these layered materials exhibit some type of charge ordering closely coupled to a more complex magnetic order. The most

famous examples are the stripe order in some cuprates and in the nickelates[13] and also the CE-type order (according to standard Wollan-Koehler notation[28]) in half-doped manganates.[15] Recently it was shown that also doped La$_{2-x}$Sr$_x$CoO₄ (Ref. 16) and La$_{1-x}$Sr$_{1+x}$MnO₄ (Ref. 17) exhibit an incommensurate magnetic ordering closely resembling the nickelate and cuprate stripe phases when the Sr content deviates from half-doping so that stripe order can be considered as a general phenomenon in cuprate and noncuprate transition-metal oxides.[18] Magnetic excitations in these complex ordered materials give a direct insight to the microscopic origin of these phases. For example, in La$_{0.5}$Sr$_{1.5}$MnO₄ one may easily associate the dominant magnetic interaction with an orbital ordering.[19] In comparison to the rather rich literature of manganates, nickelates, and cuprates, there is no knowledge about the magnon dispersion in LaSrFeO₄. We have performed an extensive study of macroscopic measurements, x-ray and neutron diffraction, as well as inelastic neutron scattering on LaSrFeO₄ single crystal and powder samples in order to address the question of eventual spin-reorientation phase transitions and to deduce the coupling constants between nearest and next-nearest neighbors within linear spin-wave theory.

II. EXPERIMENTAL

The sample preparation has been carried out similar to reported techniques.[11,20] Powder samples of LaSrFeO₄ have been prepared by mixing La₂O₃, SrCO₃, and Fe₂O₃ in the stoichiometric ratio and sintering at 1200 °C for 100 h. Diffraction patterns were taken on a Siemens D5000 x-ray powder diffractometer in order to confirm the correct phase formation (space group $I4/mmm$) and the absence of parasitic phases. Furthermore, the lattice constants were deduced at those temperatures used in the neutron study due to the higher precision of the powder method. Large single crystals of LaSrFeO₄ have been grown by the floating-zone method. Therefore, LaSrFeO₄ powder was pressed into a cylindrical rod of 60 mm length and 8 mm diameter and sintered at 1300 °C for 20 h. The crystal has been grown in a floating-zone furnace (Crystal Systems Incorporated) equipped with four halogen lamps (1000 W). The feed and seed rods were rotated in
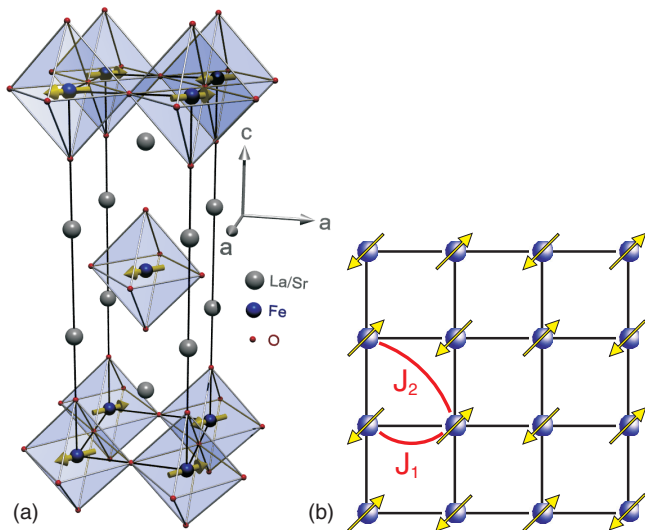
FIG. 1. (Color online) (a) Visualization of the crystal and magnetic structure of LaSrFeO$_4$. (b) Tetragonal basal plane showing only the magnetic Fe ions in order to declare the coupling constants J_1 and J_2.
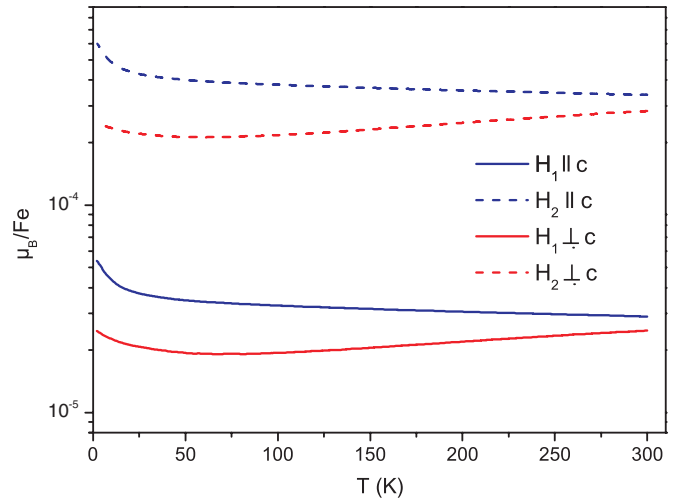

FIG. 2. (Color online) Magnetization given in Bohr magnetons per Fe atom as a function of temperature for two different applied magnetic fields parallel and perpendicular to the c axis ($H_1 = 100$, $H_2 = 1000$ Oe). No hints for a magnetic phase transition can be observed between 1.8 and 300 K.

opposite directions at about 10 rpm, while the molten zone was vertically moved at a growth speed of 3 mm/h. This procedure has been performed under a pressure of 4 bars in argon atmosphere. Suitable single crystals for x-ray diffraction have been obtained by milling larger pieces in a ball mill for several hours. The characterization at the x-ray single crystal diffractometer Bruker Apex D8 validated the successful crystal growth. The magnon dispersion has been investigated at the thermal and cold neutron triple-axis spectrometers 2T and 4F.2 at the Laboratoire Léon Brillouin (LLB) using a large single crystal of 3.33 g weight, whose single crystal state was verified by a Laue diffractometer. For energy transfers above 20 meV, inelastic data has been recorded on the 2T spectrometer, which was used with a pyrolytic graphite (PG) monochromator and a PG analyzer. The final neutron energy was fixed at either $E_f = 34.9$, $E_f = 14.7$, or $E_f = 8.04$ meV. The 4F.2 spectrometer was used with a PG double monochromator and a PG analyzer. A cooled Be filter was used to suppress higher harmonics. The final neutron energy was fixed at $E_f = 4.98$ meV. The nuclear and magnetic structure determination has been carried out at the neutron single-crystal diffractometer 5C2 (LLB) situated at the hot source of the Orphée reactor. For the elastic measurements a smaller single crystal of 39 mg has been used. A wavelength of 0.83 Å has been employed supplied by the (220) reflection of a Cu monochromator. The Néel temperature was derived at the 3T.1 spectrometer (LLB) using a furnace. Magnetization data was obtained by a commercial superconducting quantum interference device (SQUID) and a vibrating sample magnetometer (VSM). Electric resistivity has been measured by the standard four-contact method.

III. RESULTS AND DISCUSSION

A. Macroscopic properties

The magnetization data obtained from the SQUID do not show any anomalies between 1.8 and 300 K (Fig. 2) which

could have been connected to additional magnetic phase transitions as in Ref. 11. An additional measurement in a VSM with an oven did not reveal any signature of T_N in the measured range from 300 to 800 K. Such a behavior is characteristic for the layered magnetism in 214 compounds, where the ordering temperature has only been unambiguously determined by neutron diffraction experiments.[21] The fact that the Fe magnetic moments exhibit two-dimensional correlations well above T_N renders it impossible to detect this transition macroscopically. The transition from two-dimensional to three-dimensional magnetic order as well as an eventual reorientation of the antiferromagnetic spin order can however be seen via neutron diffraction. Figure 3 shows the specific resistivity as a function of temperature. No reliable data could be obtained below 175 K
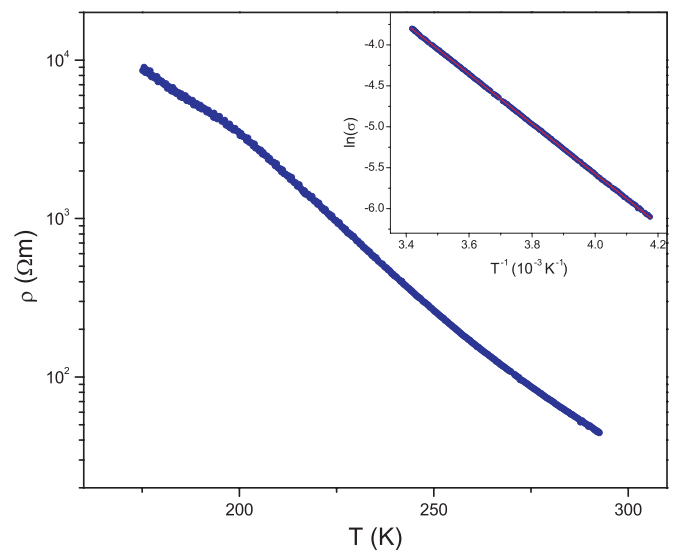

FIG. 3. (Color online) Specific resistivity of LaSrFeO$_4$ as a function of temperature. An Arrhenius fit ($\ln \sigma = \ln \sigma_0 - \frac{E}{2kT}$) to the high-temperature data yields a band gap of $\Delta = 0.525(1)$ eV.
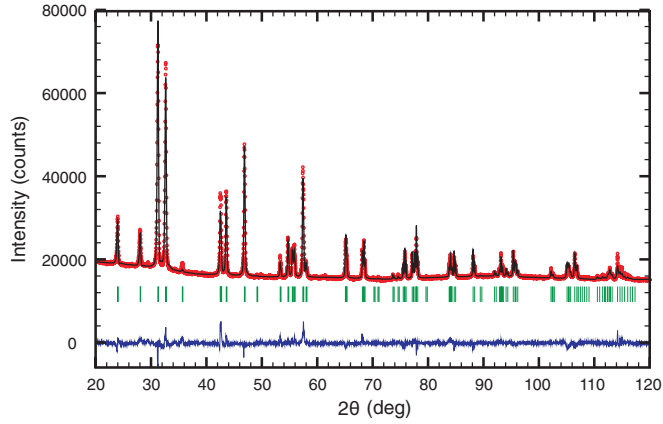
FIG. 4. (Color online) X-ray powder diffraction pattern of LaSrFeO$_4$ taken at room temperature. Raw data are depicted by (red) dots, while the calculated pattern and the difference line are represented by solid (black) and by solid (blue) lines, respectively. (Green) vertical bars indicate the position of Bragg reflections.

due to the high values of ρ. The high-temperature data has been plotted in a $\ln(\sigma)$-$\frac{1}{T}$ plot to which an Arrhenius function ($\ln \sigma = \ln \sigma_0 - \frac{E}{2kT}$) has been fitted (shown in inset). From the linear behavior a band gap of $\Delta = 0.525(1)$ eV can be deduced. At 200 K a kink is visible in the specific resistivity whose origin is not yet clear to us.

B. Nuclear structure

The investigation of the powder samples by x-ray diffraction confirmed the reported crystal structure. All powder diffraction patterns were analyzed using the FULLPROF program.[22] Figure 4 depicts the powder pattern recorded at room temperature. The calculated pattern [(black) solid line] agrees very well with the observed pattern (red dots) and

no parasitic peaks can be observed. Additional diffraction patterns were recorded at 120, 50, and 10 K. The lattice parameters have been deduced and are listed in Table I. For the nuclear structure investigation at the neutron single crystal diffractometer, a total number of 739 independent reflections has been collected at each temperature. The integrated intensities were corrected for absorption applying the transmission factor integral $\exp[-\mu(\tau_{in} + \tau_{out})]$ by using subroutines of the CAMBRIDGE CRYSTALLOGRAPHIC SUBROUTINE LIBRARY[23] (τ_{in} and τ_{out} represent the path lengths of the beam inside the crystal before and after the diffraction process, and μ is the linear absorption coefficient, which is 0.146 cm^{-1} for LaSrFeO$_4$). The nuclear structure refinement included the z value of the atomic positions of La/Sr and O2, the anisotropic temperature factors of all ions (respecting symmetry restrictions according to Ref. 24), and the occupation of the O1 and O2 site as well as the extinction parameters according to an empiric SHELX-like model.[25] All refined structural parameters are shown in Table I. The atomic positions show almost no significant dependence on the temperature, while the lattice constants and anisotropic displacement parameters (ADP) expectedly decrease with decreasing temperature. The only exception are the U_{33} parameters, which increase for all species when reducing the temperature from 50 to 10 K. This results in a much more anisotropic atomic displacement at 10 K with more out-of-plane motion. One may realize that some of the ADPs are stronger than it might be expected from the phononic contributions. It has already been pointed out in earlier studies on La$_{2-x}$Sr$_x$CuO$_4$ (Ref. 26) and La$_{1+x}$Sr$_{1-x}$MnO$_4$ (Ref. 5) that the intrinsic disorder due to the occupation of the same site by La and Sr causes a nonzero force on the oxygen ions at the mean atomic positions derived by diffraction experiments. Due to the La/Sr-O bonds being perpendicular to the Fe-O bonds, the disorder will affect the displacement of the O ions mainly perpendicular to the Fe-O bonds, i.e., the U_{33} parameter of O1 and the U_{11} parameter of O2 are most affected. The refinement

TABLE I. Nuclear structure parameters within the $I4/mmm$ space group at different temperatures. The Wyckoff sites are La/Sr $4e$ $(00z)$, Fe $2a$ (000), O1 $4c$ $(0\frac{1}{2}0)$, and O2 $4e$ $(00z)$. The results of the neutron single crystal diffraction experiment were completed by measuring the lattice constants using x-ray powder diffraction. For La/Sr, Fe, and O2, U_{22} is constrained by symmetry to U_{11}.

	T (K)	10 K	50 K	120 K	RT
	a (Å)	3.8709(1)	3.8713(1)	3.8726(1)	3.8744(1)
	c (Å)	12.6837(4)	12.6848(4)	12.6931(4)	12.7134(3)
La/Sr	z	0.3585(1)	0.3589(1)	0.3589(1)	0.3587(1)
	U_{11} (Å^2)	0.0032(6)	0.0056(5)	0.0067(5)	0.0107(5)
	U_{33} (Å^2)	0.007(1)	0.0045(4)	0.0044(4)	0.0089(5)
Fe	U_{11} (Å^2)	0.0017(7)	0.0036(4)	0.0047(4)	0.0069(6)
	U_{33} (Å^2)	0.013(1)	0.0099(5)	0.0121(5)	0.0186(7)
O1	occ (%)	99(2)	102(2)	102(2)	99(2)
	U_{11} (Å^2)	0.0050(9)	0.009(1)	0.007(2)	0.011(1)
	U_{22} (Å^2)	0.0034(9)	0.003(2)	0.006(2)	0.0074(9)
	U_{33} (Å^2)	0.012(1)	0.0085(4)	0.0097(5)	0.0175(9)
O2	occ (%)	97(2)	97(2)	97(2)	96(2)
	z	0.1694(2)	0.1686(1)	0.1689(1)	0.1692(2)
	U_{11} (Å^2)	0.0160(9)	0.0160(4)	0.0179(7)	0.0230(8)
	U_{33} (Å^2)	0.011(1)	0.0079(7)	0.0077(6)	0.0124(7)
	R_F (%)	2.65	2.84	3.17	2.78
	χ^2	0.33	2.35	2.05	4.60

indeed yields pronounced enhancement of these parameters. From the neutron data an eventual oxygen deficiency might be deduced. Taking into account the refinement with the best agreement factors, one can calculate the stoichiometry of the investigated compound to be $LaSrFeO_{3.92(6)}$ yielding a slight oxygen deficiency.

C. Magnetic structure

We found strong half-indexed magnetic Bragg peaks confirming the known propagation vector $\mathbf{q}_1 = (\frac{1}{2}\frac{1}{2}0)$. The intensity of the magnetic $(\frac{1}{2}\frac{1}{2}0)$ reflection was measured as a function of temperature and is shown in Fig. 5. A power-law fit to the integrated intensity data yields a Néel temperature of 366(2) K and a critical exponent $\beta = 0.15(5)$ (upper right inset). However, an exact determination of T_N is hardly possible as significant intensity due to strong quasielastic scattering can be observed well above the transition temperature, e.g., at 400 or 460 K. By scanning across the forbidden (010) reflection an eventual $\lambda/2$ contamination can be ruled out (upper left inset).

As two additional magnetic phase transitions might be expected at 90 and 30 K (Refs. 11 and 12), the magnetic structures have been investigated at 120, 50 and 10 K. For the magnetic structure refinement a total number of 185 independent reflections has been recorded at each temperature point, where the integrated intensities have been corrected for absorption. Representation analysis has been used to derive symmetry adapted spin configurations which were then refined to the respective data. Three irreducible representations are compatible with the space group $I4/mmm$ yielding collinear spin configurations with the moments parallel to the c axis, parallel to $\mathbf{q}$ or perpendicular to $\mathbf{q}$, the last two being of orthorhombic symmetry.[27] Due to the fact that $\mathbf{q}_2 = (-\frac{1}{2}\frac{1}{2}0)$ is a possible propagation vector as well, each of the irreducible

FIG. 6. (Color online) Magnetic G-type ordering (according to standard Wollan-Koehler notation[28]) in $LaSrFeO_4$ only showing the magnetic Fe ions and their spins for the two $\mathbf{q}$ domains. (a) shows the irreducible representation labeled $G_x - G_y$ which has the magnetic moments perpendicular to $\mathbf{q}_1$ (left) and $\mathbf{q}_2$ (right). (b) shows the irreducible representation labeled $G_x + G_y$ with the magnetic moments parallel to $\mathbf{q}_1$ (left) and $\mathbf{q}_2$ (right).

representations with the basis vectors in the a-b plane will exhibit two magnetic orientations. The domains are connected to each other by the symmetry operator $(y,-x,z)$ which has been lost during the transition into the magnetically ordered state. The relevant spin configurations used in previous analyses[6,12] are shown in Fig. 6.

The data could well be described by the model $G_x - G_y$, where the size and the direction (angle ϕ between the moment and the a axis) of the magnetic moments in the basal plane as well as the percental distribution between the two magnetic domains were refined. The results are listed in Table II for all investigated temperatures. In Refs. 6 and 12 the authors claim that their sample exhibits an inhomogeneous distribution of the two collinear representations $G_x - G_y$ and $G_x + G_y$ accounting for 92% and 8% of the sample volume. Furthermore, the intensity jumps of characteristic magnetic Bragg reflections at the transition temperatures 30 and 90 K were attributed to a change in the relative distribution of the representations. We have followed the integrated intensity of characteristic magnetic Bragg reflections as a function of temperature across the two lower magnetic phase transitions and could not observe any significant jumps (Fig. 7). Although the statistics seem to be limited in comparison to the size of the jumps at least for the (0.5 0.5 1) reflection, one can state that the scattering from both domains does not exhibit contrary behavior in dependence on temperature ruling out
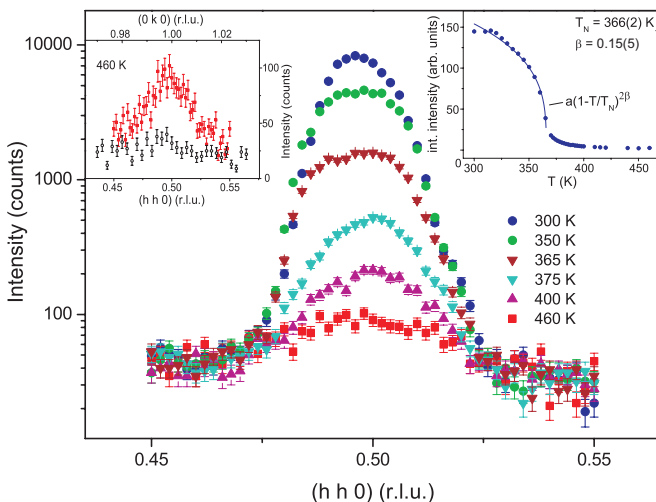

FIG. 5. (Color online) Longitudinal $\mathbf{q}$ scan across the magnetic $(\frac{1}{2}\frac{1}{2}0)$ reflection (the intensity is plotted on a $\log_{10}$ scale). The inset at the upper right shows the integrated intensity as a function of temperature. A power-law fit yields a T_N of 366(2) K. The inset at the upper left depicts the same longitudinal $\mathbf{q}$ scan at 460 K [(red) filled squares] together with a longitudinal $\mathbf{q}$ scan across the forbidden (010) reflection [(black) open circles] documenting that no $\lambda/2$ contamination is present.
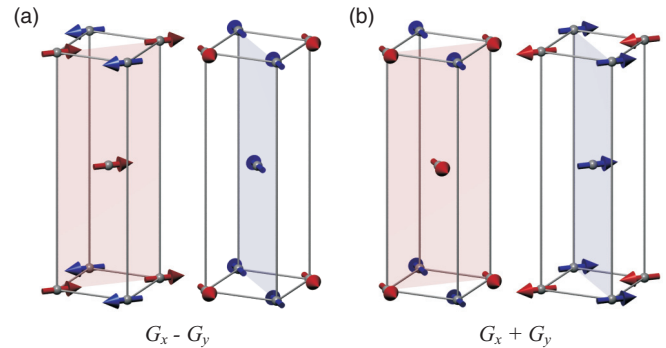
TABLE II. Results of the magnetic structure refinement.

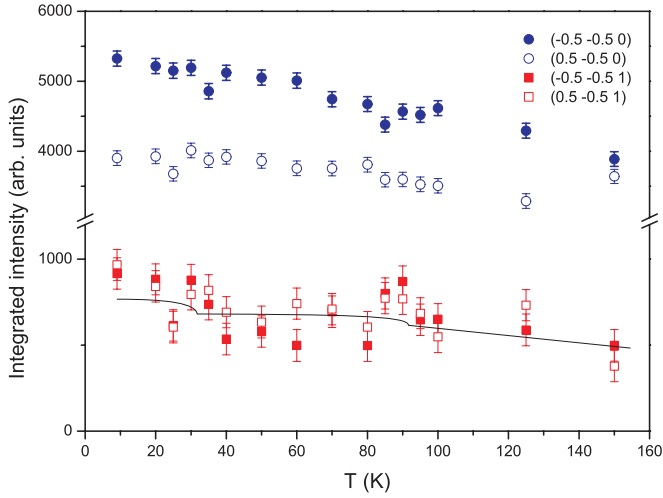| T (K)	10 K	50 K	120 K
m_{Fe} (μ_B)	4.96(1)	5.38(1)	5.09(1)
ϕ (deg)	44.0(8)	44.9(8)	46.7(8)
domain $\mathbf{q}_1$ (%)	46.5(4)	47.3(4)	47.7(5)
domain $\mathbf{q}_2$ (%)	53.5(4)	52.7(4)	52.3(5)
$G_x - G_y$ (%)	98(2)	97(2)	98(2)
$G_x + G_y$ (%)	2(2)	3(2)	2(2)
R_F (%)	5.14	4.43	4.76
χ^2	1.78	1.75	1.95

FIG. 7. (Color online) Integrated intensity of characteristic magnetic Bragg reflections probing either domain $\mathbf{q}_1$ (positive h values) or domain $\mathbf{q}_2$ (negative h values) as a function of temperature. The solid line represents the size of the jumps reported in Ref. 12.

a redistribution of domain population. We have applied the proposed inhomogeneous distribution of two representations to our data; however, no significant contribution of $G_x + G_y$ is present (see Table II).

D. Magnon dispersion

The magnon dispersion has been investigated at 10 K along the two main-symmetry directions $[0\ \xi\ 0]$ and $[\xi\ \text{-}\xi\ 0]$. Depending on the orientation of the resolution ellipsoid with respect to the dispersion branch, constant-$\mathbf{Q}$ or constant-E scans have been performed. The excitation signals have been fitted with two symmetrical Gaussian functions (constant-$\mathbf{Q}$ scans) or an asymmetric double sigmoid[29] (constant-E scans) in order to account for the strong asymmetry at high energy transfers. An asymmetry has been applied to the symmetric Gaussian functions for the constant-$\mathbf{Q}$ scans at higher energy transfer. Exemplary scans are shown in Fig. 8 documenting the data analysis.

According to the magnetic structure, where the magnetic moments are lying in the tetragonal basal plane, two gapped excitations have to be expected. The lower one should be connected to the amount of energy needed to turn a spin out of its ordered position within the basal plane whereas the higher one results from turning a spin out of the plane. Constant-$\mathbf{Q}$ scans have been performed at different Brillouin zone centers in order to derive the size of the respective spin gaps. In Figs. 9(a) to 9(c) a clear signal can be observed at 5.26(2) meV [the value has been obtained from an asymmetric double-sigmoid fit to the scan at $\mathbf{Q} = (1.5\ 0.5\ 0)$], which we identify as the higher-lying out-of-plane gap Δ_{out}. In Fig. 9(c) an additional signal appears at 8.5(2) meV which, however, is not present in the lower zone center scans and therefore rather phononic than magnetic. It can be seen especially in Figs. 9(a) and 9(b) that the scattered intensity is not reduced to the background below Δ_{out}. Bearing in mind the energy resolution of 0.23 meV as obtained from the full width at half maximum (FWHM) of the elastic line, we conclude that the
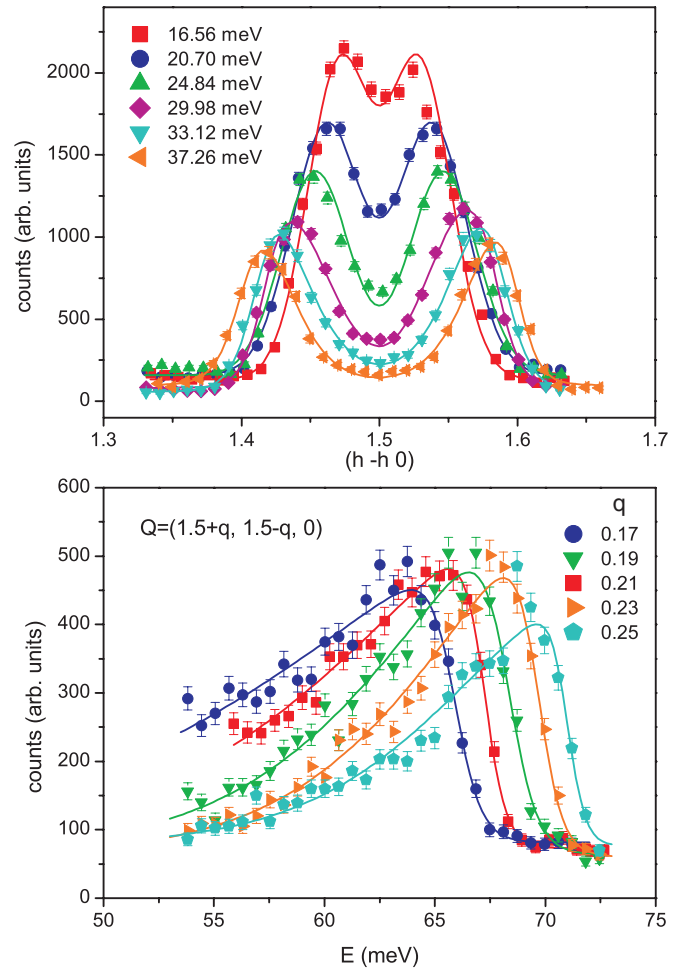

FIG. 8. (Color online) Exemplary scans showing how the values of $S(q,\omega)$ have been obtained. Constant-E scans have been fitted with two symmetric Gaussian functions (upper plot), while constant-$\mathbf{Q}$ scans have been fitted with asymmetric double sigmoids (lower plot).

scattered intensity at low energy originates from the in-plane fluctuation of the magnetic moments. Due to the finite size of the resolution ellipsoid and its inclination in $S(q,\omega)$, space signals from steep dispersion branches become very broad as can be seen in Fig. 9(b), where considerable scattered intensity is observed well above 10 meV. For this reason we expect the in-plane fluctuations to be gapless.

Within linear spin-wave theory we used a Hamiltonian of a Heisenberg antiferromagnet with isotropic nearest (J_1) and next-nearest neighbor (J_2) interactions [see Fig. 1(b)] as well as an effective magnetic anisotropy field H_A along the z axis:[30]

$$H = \sum_{\mathbf{m,r}} J_1(\mathbf{r})\mathbf{S_m} \cdot \mathbf{S_{m+r}} + \sum_{\mathbf{m,R}} J_2(\mathbf{R})\mathbf{S_m} \cdot \mathbf{S_{m+R}}$$

$$+ \sum_{\mathbf{n,R}} J_2(\mathbf{R})\mathbf{S_n} \cdot \mathbf{S_{n+R}} + g\mu_B H_A \left(\sum_m S_\mathbf{m}^z - \sum_n S_\mathbf{n}^z \right).$$

$$(1)$$

Here the magnetic lattice has been divided into two identical sublattices m and n where each of them only contains parallel spins. $\mathbf{r}$ is a connection vector between magnetic moments of the interpenetrating antiferromagnetically coupled (J_1)
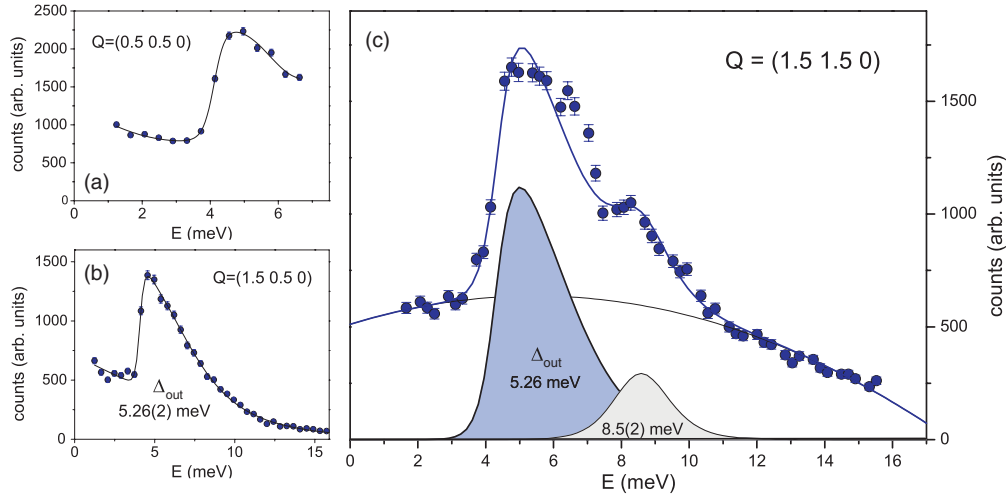
FIG. 9. (Color online) Constant-**Q** scans at the magnetic zone centers (a) (0.5 0.5 0), (b) (1.5 0.5 0), and (c) (1.5 1.5 0). The excitations have been fitted by asymmetric double sigmoid functions on a polynomial background. The out-of-plane anisotropy gap amounts to 5.26(2) meV as obtained by a fit to the data in panel (b). In panel (c) the signal at 8.5(2) meV is presumably phononic as the same scan at lower **Q** values, see panel (b), is featureless at this energy. Δ_{out} has been held constant in the fit to the data shown in panel (c). The fit curve in panel (a) serves as a guide to the eye. The considerable scattered intensity below Δ_{out} is a hint for the lower-lying in-plane excitation.

sublattices with respective positions **m** and **n**, while **R** denotes a connection vector between two ferromagnetically coupled magnetic moments of the same sublattice (J_2). Each spin pair contributes only once to the sum. The diagonalization of the Hamiltonian[30] leads to the dispersion relation for this particular crystal structure:

$$\hbar\omega_q = (\{4SJ_1 - 4SJ_2[1 - \cos(2\pi q_x)\cos(2\pi q_y)]$$
$$+ g\mu_B H_A\}^2 - (2SJ_1)^2[\cos(2\pi q_x) + \cos(2\pi q_y)]^2)^{\frac{1}{2}}. \quad (2)$$

We have fitted the dispersion relation simultaneously to spin waves propagating along $[0\,\xi\,0]$ and $[\xi\,\text{-}\xi\,0]$. With an expected $S = 2.5$ we obtain $J_1 = 7.4(3)$ meV, $J_2 = 0.4(3)$ meV, and $\mu_B H_{A,out} = 0.097(6)$ meV (note that a factor 2 has been added to the J values for a correct comparison with Refs. 31–34 due to a different definition of the sums in the Hamiltonian). The agreement with the experimental data is fairly good; the dispersion curve is depicted as a (black) solid line in Fig. 10. Setting $J_2 = 0$ yields $J_1 = 6.99(4)$ and $\mu_B H_{A,out} = 0.102(5)$ meV, and the agreement is comparable [(red) dashed line in Fig. 10]. While along $[\xi\,\text{-}\xi\,0]$ the dispersion is practically unchanged, it goes to higher energy values at the zone boundary for the propagation along $[0\,\xi\,0]$, however, staying within the error bars of the data points. The fact that J_2 is not essentially needed to describe the dispersion makes it possible to apply the spin-wave dispersion reported in Ref. 35, which has been derived for the isostructural K_2FeF_4 structure. This spin Hamiltonian for Fe^{2+} in a tetragonally distorted cubic crystal field only contains a nearest-neighbor exchange parameter, but considers two nondegenerate spin-wave dispersion branches, which—in a semiclassical picture—correspond to elliptical precessions of the spins with the long axis of the ellipse either in or perpendicular to the layer.[35] The spin-wave dispersion is

given in Eq. (3) for the larger orthorhombic cell:

$$\hbar\omega_q = 4S|J|[(1 + A)^2$$
$$- (\cos[\pi(q_x + q_y)]\cos[\pi(q_x - q_y)] \pm B)^2]^{\frac{1}{2}}, \quad (3)$$

with $A = (D - 3E)/(4|J|)$ and $B = (D + E)/(4|J|)$. D is a parameter describing the uniaxial anisotropy and E adds an in-layer anisotropy. Fitting Eq. (3) with $E = 0$ to both data sets simultaneously yields the values $J = 7.00(4)$ meV and $D = 0.041(2)$ meV. The two nondegenerate branches are depicted as white solid lines in Fig. 10. The upper branch coincides
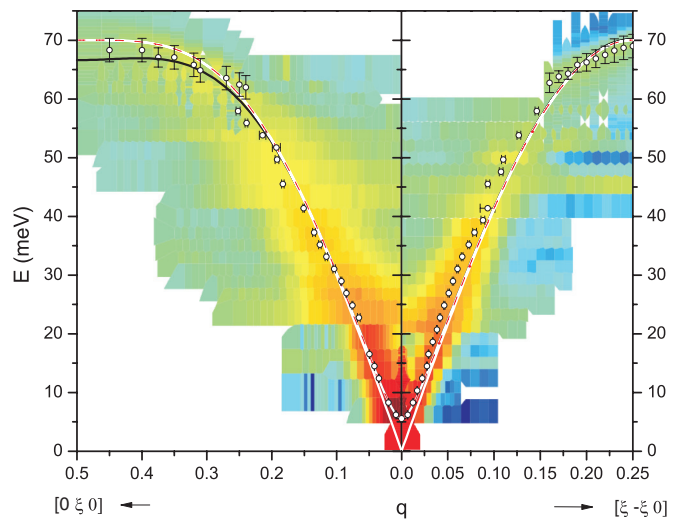

FIG. 10. (Color online) Two-dimensional reconstruction of $S(q,\omega)$ along the two symmetry directions $[0\,\xi\,0]$ and $[\xi\,\text{-}\xi\,0]$ from all constant-**Q** and constant-E scans as exemplarily shown in Fig. 8. Dots mark the peak center as obtained from the fits to the raw data. The straight white line is a fit of the dispersion relation [Eq. (2)] to both data sets simultaneously.

exactly with the formalism in Eq. (2) (only nearest-neighbor interaction) yielding the same coupling constant within the error bars. The lower branch is gapless as predicted by $E = 0$ and the reason for the nonzero intensity below Δ_{out} in Fig. 9.

An examination of the energy gaps as a function of temperature yielded no differences between 10 and 100 K.

IV. CONCLUSION

We have conducted a comprehensive study on the single-layered perovskite LaSrFeO$_4$. Our x-ray powder and single crystal diffraction as well as Laue diffraction yield high sample quality, while our magnetization data differ from previously published work. Detailed investigation of the nuclear structure by neutron diffraction on a single crystal reveals that the intrinsic disorder on the La/Sr site leads to a stronger atomic displacement of the O1 and O2 ions in LaSrFeO$_4$ in analogy to La$_{1+x}$Sr$_{1-x}$CuO$_4$ (Ref. 26) and La$_{1+x}$Sr$_{1-x}$MnO$_4$ (Ref. 5). The main results of our study concern the magnetic structure and the magnon dispersion of this compound, which we analyzed by neutron diffraction and inelastic neutron scattering. We have addressed the open question concerning the magnetic phase transitions at 90 and 30 K. Our SQUID data did not yield any hint for additional magnetic phase transitions and based on our neutron diffraction data we are able to say that no spin reorientation or domain/representation redistribution is present. Possible discrepancies between the data of different studies might be the exact amount of oxygen as these systems are known to exhibit oxygen deficiency. From the nuclear structure refinement we can deduce the oxygen deficiency to be $y = 0.08(6)$ in LaSrFeO$_{4-y}$. The large number of measured reflections allows an analysis of the magnetic form factor. Therefore, the observed magnetic structure factors were divided by the exponential part of the calculated magnetic structure factor and the ordered moment. The resulting observed magnetic form factor has been derived for (hk0) and (hkl) reflections in order to gain information about the in-plane and out-of-plane atomic magnetization density distribution in LaSrFeO$_4$. In Fig. 11 the observed magnetic form factors for both kinds of magnetic reflections are depicted showing a tendency towards a weaker decrease with increasing $\sin(\theta)/\lambda$ in comparison to the tabulated analytical approximation of the Fe^{3+} magnetic form factor, which would imply a more localized atomic magnetization density distribution. However, due to the limited number of (hk0) reflections and the size of the error bars, no significant anisotropy can be deduced.

In addition, we have analyzed the magnon dispersion along the two symmetry directions $[0\ \xi\ 0]$ and $[\xi\ -\xi\ 0]$. Within linear spin-wave theory we can describe both branches with the nearest-neighbor and next-nearest neighbor interaction $J_1 = 7.4(3)$ meV and $J_2 = 0.4(3)$ meV, respectively ($S = 2.5$). These values are more than a factor 2 larger than those in the isostructural undoped LaSrMnO$_4$ with $S = 2$ (Ref. 31), which can be attributed to the fact that e_g-e_g superexchange contributes only little for the case of the Mn orbital arrangement in LaSrMnO$_4$. Our data indicate two nondegenerate spin-wave dispersion branches. A clear signal at 5.26(2) meV was identified as the out-of-plane anisotropy gap Δ_{out}. The nonzero scattered intensity at lower energy transfers is explained by the lower-lying anisotropy gap,
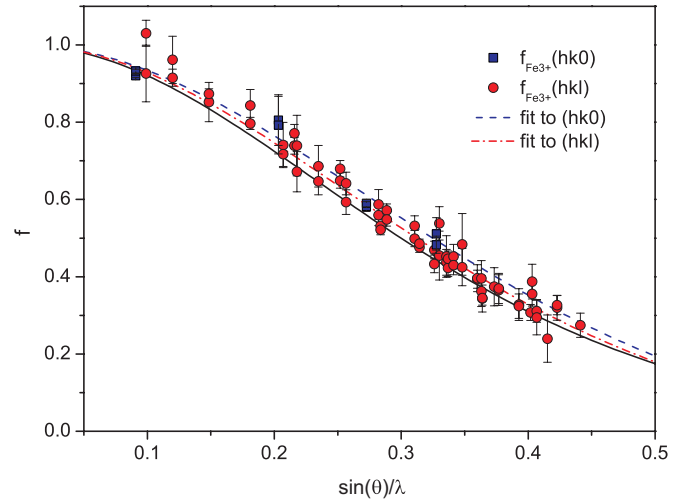

FIG. 11. (Color online) Observed magnetic Fe form factor for (hk0) [(blue) squares] and (hkl) [(red) dots] magnetic reflections. The (black) solid line depicts the tabulated analytical approximation of the Fe^{3+} form factor. The data have been fitted by varying the tabulated values while requiring $f(0) = 1$ [(red) dash-dotted line is the fit to the (hkl) data; (blue) dashed line is the fit to the (hk0) data].

which was then analyzed by using the formalism described in Ref. 35. With a nearest-neighbor interaction $J = 7.00(4)$ meV and the anisotropy parameters $D = 0.041(2)$ and $E = 0$, a good agreement between the upper dispersion branch and the experimental data has been achieved, while the lower branch goes down to zero-energy transfer at the magnetic zone center. The spin-wave dispersion in La$_2$NiO$_4$ is also well described by a nearest-neighbor interaction only,[32] but with $J = 31$ meV it is a factor of 4 stronger than in LaSrFeO$_4$ indicating higher hybridization in La$_2$NiO$_4$. Although a more involved Hamiltonian has been used for the description of the spin dynamics in La$_2$CoO$_4$ (with high-spin $S = \frac{3}{2}$ Co^{2+}) including three coupling constants and corrections for spin-orbit coupling, ligand and exchange fields,[33] the resulting coupling constants are of the same order as the ones presented here. Furthermore, the out-of-plane gap and the bandwidth are quite comparable. In order to compare the single-ion anisotropy of the involved species within one model we have used Eq. (2) together with the J values given in Refs. 31–34 (up to next-nearest neighbor exchange) to calculate the anisotropy parameter $\mu_B H_{A,\mathrm{out}}$. The approximate values of the dispersion at the zone center and zone boundary were taken from plots within Refs. 31–34. The comparison of J and $H_{A,\mathrm{out}}$ for the different compounds is shown in Table III.

TABLE III. Comparison of the exchange coupling and anisotropy parameters of LaSrFeO$_4$ with the other 214 compounds [LaSrMnO$_4$ (Ref. 31), La$_2$CoO$_4$ (Ref. 33), La$_2$NiO$_4$ (Ref. 32), and La$_2$CuO$_4$ (Ref. 34)].

	Mn	Fe	Co	Ni	Cu
S	2	2.5	1.5	1	0.5
J_1 (meV)	3.4(3)	7.4(3)	9.69(2)	31	104(4)
J_2 (meV)	0.4(1)	0.4(3)	0.43(1)	0	−18(3)
$\mu_B H_{A,\mathrm{out}}$ (meV)	0.65	0.097(6)	0.67	0.52	0

One can see that the single-ion anisotropy of the Fe^{3+} in $LaSrFeO_4$ is significantly smaller than in the other 214 compounds (except for La_2CuO_4), which is expected due to the close to zero orbital moment and therefore very weak spin-orbit coupling.

*Corresponding author: qureshi@ph2.uni-koeln.de

†braden@ph2.uni-koeln.de

[1] S. N. Ruddlesden and P. Popper, Acta Crystallogr. **10**, 538 (1957).

[2] S. Jin, T. H. Tiefel, M. McCormack, R. A. Fastnacht, R. Ramesh, and L. H. Chen, Science **264**, 413 (1994).

[3] S. Kawano, N. Achiwa, N. Kamegashira, and M. Aoki, J. Phys. Colloques **49**, C8 (1988).

[4] P. Reutler, O. Friedt, B. Büchner, M. Braden, and A. Revcolevschi, J. Cryst. Growth **249**, 222 (2003).

[5] D. Senff, P. Reutler, M. Braden, O. Friedt, D. Bruns, A. Cousson, F. Bourée, M. Merz, B. Büchner, and A. Revcolevschi, Phys. Rev. B **71**, 024425 (2005).

[6] J. L. Soubeyroux, P. Courbin, L. Fournes, D. Fruchart, and G. le Flem, J. Solid State Chem. **31**, 313 (1980).

[7] K. Yamada, M. Matsuda, Y. Endoh, B. Keimer, R. J. Birgeneau, S. Onodera, J. Mizusaki, T. Matsuura, and G. Shirane, Phys. Rev. B **39**, 2336 (1989).

[8] D. Vaknin, S. K. Sinha, D. E. Moncton, D. C. Johnston, J. M. Newsam, C. R. Safinya, and H. E. King, Phys. Rev. Lett. **58**, 2802 (1987).

[9] J. Rodríguez-Carvajal, M. T. Fernandez-Díaz, and J. L. Martínez, J. Phys.: Condens. Matter **3**, 3215 (1991).

[10] K. Yamada, T. Omata, K. Nakajima, S. Hosoya, T. Sumida, and Y. Endoh, Physica C **191**, 15 (1992).

[11] C. Bansal, H. Kawanaka, H. Bando, A. Sasahara, R. Miyamoto, and Y. Nishihara, Solid State Commun. **128**, 197 (2003).

[12] M. H. Jung, A. M. Alsmadi, S. Chang, M. R. Fitzsimmons, Y. Zhao, A. H. Lacerda, H. Kawanaka, S. El-Khatib, and H. Nakotte, J. Appl. Phys. **97**, 10A926 (2005).

[13] M. Imada, A. Fujimori, and Y. Tokura, Rev. Mod. Phys. **70**, 1039 (1998).

[14] D. Senff, Master's thesis, University of Köln, 2003.

[15] I. A. Zaliznyak, J. P. Hill, J. M. Tranquada, R. Erwin, and Y. Moritomo, Phys. Rev. Lett. **85**, 4353 (2000).

[16] M. Cwik, M. Benomar, T. Finger, Y. Sidis, D. Senff, M. Reuther, T. Lorenz, and M. Braden, Phys. Rev. Lett. **102**, 057201 (2009).

[17] H. Ulbrich, D. Senff, P. Steffens, O. J. Schumann, Y. Sidis, P. Reutler, A. Revcolevschi, and M. Braden, Phys. Rev. Lett. **106**, 157201 (2011).

[18] H. Ulbrich and M. Braden, Physica C **481**, 31 (2012).

[19] D. Senff, F. Krüger, S. Scheidl, M. Benomar, Y. Sidis, F. Demmel, and M. Braden, Phys. Rev. Lett. **96**, 257201 (2006).

[20] K. Oka and H. Unoki, J. Cryst. Growth Soc. Jpn. **14**, 183 (1987).

[21] D. Senff, O. Schumann, M. Benomar, M. Kriener, T. Lorenz, Y. Sidis, K. Habicht, P. Link, and M. Braden, Phys. Rev. B **77**, 184413 (2008).

[22] J. Rodríguez-Carvajal, Physica B **192**, 55 (1993).

[23] J. C. Matthewman, P. Thompson, and P. J. Brown, J. Appl. Crystallogr. **15**, 167 (1982).

[24] W. J. A. M. Peterse and J. H. Palm, Acta Crystallogr. **20**, 147 (1966).

[25] A. C. Larson, in *Crystallographic Computing*, edited by F. R. Ahmed, S. R. Hall, and C. P. Huber (Munksgaard, Copenhagen, 1970), pp. 291–294.

[26] M. Braden, M. Meven, W. Reichardt, L. Pintschovius, M. T. Fernandez-Diaz, G. Heger, F. Nakamura, and T. Fujita, Phys. Rev. B **63**, 140510(R) (2001).

[27] As the magnetic structure possesses orthorhombic symmetry it might be expected that the crystal structure reacts to the onset of magnetism by an orthorhombic distortion. Therefore, additional high resolution powder diffraction data have been collected using synchrotron radiation (B2, HASYLAB). However, no peak splitting could be observed within the instrumental resolution.

[28] E. O. Wollan and W. C. Koehler, Phys. Rev. **100**, 545 (1955).

[29] The asymmetric double-sigmoid function $I = bgr + A[1 + \exp(-\frac{x-x_c+w_1/2}{w_2})]^{-1}\{1 - [1 + \exp(-\frac{x-x_c-w_1/2}{w_3})]^{-1}\}$ makes it possible to describe asymmetric peak profiles with unequal parameters w_2 and w_3.

[30] W. Marshall and S. Lovesey, *Theory of Thermal Neutron Scattering* (Oxford University Press, Oxford, 1971).

[31] S. Larochelle, A. Mehta, L. Lu, P. K. Mang, O. P. Vajk, N. Kaneko, J. W. Lynn, L. Zhou, and M. Greven, Phys. Rev. B **71**, 024435 (2005).

[32] K. Nakajima, K. Yamada, S. Hosoya, T. Omata, and Y. Endoh, J. Phys. Soc. Jpn. **62**, 4438 (1993).

[33] P. Babkevich, D. Prabhakaran, C. D. Frost, and A. T. Boothroyd, Phys. Rev. B **82**, 184425 (2010).

[34] R. Coldea, S. M. Hayden, G. Aeppli, T. G. Perring, C. D. Frost, T. E. Mason, S.-W. Cheong, and Z. Fisk, Phys. Rev. Lett. **86**, 5377 (2001).

[35] M. P. H. Thurlings, E. Frikkee, and H. W. de Wijn, Phys. Rev. B **25**, 4750 (1982).